December 2019

Porous Silicon Photonics at Unity Confinement Factors for Surface Adlayer Biosensing

Tahmid Hassan Talukdar
Clemson University, ttalukd@clemson.edu

POROUS SILICON PHOTONICS AT UNITY CONFINEMENT FACTORS FOR SURFACE ADLAYER BIOSENSING

A Thesis
Presented to
the Graduate School of
Clemson University

In Partial Fulfillment
of the Requirements for the Degree
Master of Science
Electrical Engineering

---

by
Tahmid Hassan Talukdar
December 2019

Accepted by:
Dr. Judson D. Ryckman, Committee Chair
Dr. William R. Harrell
Dr. Taufiquar Khan

ABSTRACT

Guided wave-optics is an emergent platform for label free optical biosensing. However, device sensitivity toward surface-attached biomolecules is directly restricted because of only evanescent interaction and low modal overlap with the active sensing region. In this work, we demonstrate a mesoporous silicon waveguide design created via a novel inverse processing technique that overcomes the limitations imposed by evanescent field sensing by achieving maximal transverse confinement factor in the active sensing region. Our sensor can also maintain this confinement factor and sensitivity across a large dimensional variation while preserving single-mode operation. Our devices are characterized in a Fabry-Perot interferometer configuration and the ultra-high sensitivity to small molecule adlayers is shown. We also discover dispersion to be a promising degree of freedom for exceeding the bulk sensitivity limits predicted by non-dispersive and isotropic effective medium theory.

To my wife

ACKNOWLEDGMENTS

First and foremost, I would like to thank my advisor and mentor Dr. Judson D. Ryckman without whose guidance and advice, this work would not be possible. I believe working under a strong researcher like him has not only built my foundation as a researcher, but also dramatically improved my theoretical, experimental, programming, and writing skills. Since joining his research group in Fall 2017, I've had the opportunity to push myself beyond my intellectual limits with various interesting and challenging projects which was and still is exhilarating. Throughout my time as a graduate student, I never felt stuck - even when I was making no progress over weeks - because of his presence, advice and an open door. He is truly the best advisor one could ask for.

Second, I wish to thank Ivan Kravchenko from Oak Ridge National Lab for making the fabrication process so effortless and teaching me my way around the CNMS cleanroom. He is indeed a vibrant and lively guy who makes my trips to ORNL so much more enjoyable. I'd like to note that a portion of this research was conducted at the Center for Nanophase Materials Sciences, which is a DOE Office of Science User Facility. I would also like to thank Gabriel D. Allen for his earlier contributions to this work.

Many thanks to my colleagues Farhan Bin-Tarik, Nazmus Sakib and Cody Nelson for their friendship and support. I'd also like to thank Ethan Kirkland, Grayson Glanton and Rachella Mariano for being so friendly and welcoming to me as the first graduate student arriving in the U.S. in this group. I profusely thank my committee members Dr.

Harrell and Dr. Khan for being there for me and also the faculty and staff members of Holcombe Department of Electrical Engineering for all their help and support.

I would like to thank my parents and my little brother for their endless support and love. Thanks to my grandmas and grandpas for spoiling me enough to fly over 8000 miles away from home to pursue my interests. Special thanks to my wife Farah for putting up with me and my obsession with work and other hobbies.

Finally, I'd like to thank the Almighty for making everything possible, for giving me the strength to attempt to push the boundaries of human knowledge and giving me a chance to make a difference in the world.

TABLE OF CONTENTS

Page

Table of Contents (Continued) Page

LIST OF TABLES

LIST OF FIGURES

LIST OF SYMBOLS

n_A	local refractive index (RIU)
n_{eff}	effective index (RIU)
n_g	group index (RIU)
S_1	effective index sensitivity for refractive index change
S_2	effective index sensitivity for adlayer attachment (RIU/nm)
S_3	group index sensitivity for adlayer attachment (RIU/nm)
S	wavelength shift per adlayer attachment (nm/nm)
Γ_A	transverse confinement factor
E	electric field
dxdy	differential area
λ	wavelength
ε	permittivity of the medium (F/m)
σ	adlayer thickness (nm)
n_{core}	refractive index in the core region (RIU)
$n_{cladding}$	refractive index in the cladding region (RIU)
L	length of waveguide
R_1, R_2	Fresnel reflectivities

CHAPTER ONE

INTRODUCTION

1.1 Overview of Biosensors

A biosensor can be defined as a device that transforms chemical information to a measurable signal that contains information of the presence and/or concentration of a specific molecule. These sensors can be broken down into two systems: one system that recognizes a specific chemical/biomolecule and one system that acts as the physico-chemical transducer. Here, the target molecule is called the *analyte*. The method of detection is called a *bioassay*. This involves a recognition system that can translate the analyte concentration to a signal with a defined sensitivity. It's also required that the sensor can reject any signal generated by molecules other than the target analyte [1].

Biosensors can be classified in various ways: method of detection, sample delivery methods, analyte monitoring methods etc. Modern biosensing platforms employ various methods of detection: optical [2], electrochemical, thermometric, piezoelectric and magnetic [3,4]. Here, sensors may be divided into two major categories: labelled and label-free. Labelling requires the target analyte to be labeled with a particular chemical compound that interacts or amplifies the analyte's interaction with the sensor device. This is an indirect way of detecting the analyte by detecting the label attached to it instead. Label-free detection method is a more direct approach that detects the analyte itself without needing any labels. Among various biosensing methods, optical biosensing offers distinct advantages owing to the higher sensitivity, selectivity, cost effectiveness, smaller form factor and the choice of being label free. Guided mode optics in particular has shown

promise in a variety of technologies, such as: surface plasmon resonance (SPR) [5], guided mode resonance (GMR) [6], nanophotonic waveguides and resonators [7–9], 2D atomic materials [10], fiber optic biosensors [11], whispering gallery resonators [12], and many more [13]. The working principle of an optical biosensor is illustrated in figure 1.

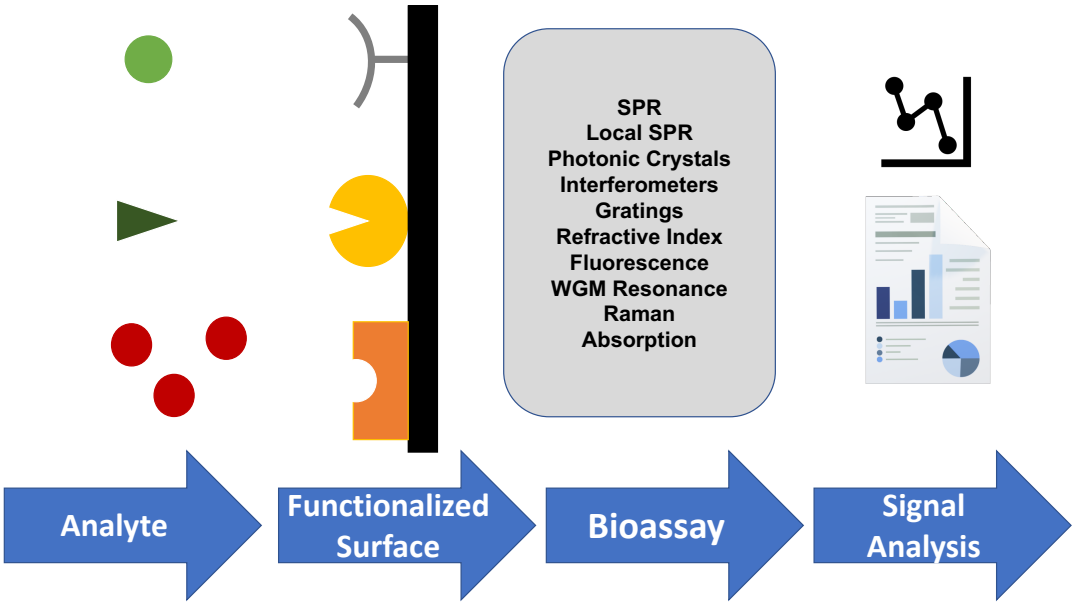

Figure 1. Working principle of an optical biosensor

1.2 Specific detection of target analytes

A key feature of a biosensor is specific detection of the target analyte. This may mean the biosensor ignores signals from attached molecules other than the analyte, or to ignore interaction / binding with molecules other than the analyte in the first place. Either option can be utilized, although the latter is a much simpler and more straightforward approach. The sensor described in our work works in this principle. To reject binding with

any molecule other than the analyte, the sensor must be functionalized in such a way that it only interacts with the analyte. This may be achieved using specific surface chemistry.

The attachment between two biomolecules that has very high affinity and exclusivity is called specific binding. This is often attributed to a molecule having a geometric match that acts as a pocket to which the other molecule can bind. The binding can also be affected by pH, positive and negatives forces between the molecules and the overall energy of the biochemical system. It is also possible for unwanted biomolecules to be attached to the sensor surface which would generate a detection signal. This kind of attachment is called nonspecific binding. It's a goal to keep in mind when designing a biosensor that nonspecific binding is to be minimized. It is possible to develop surface chemistry robust enough to allow very specific detection of molecules in our case of surface based optical sensing platforms.

1.3 Sensor functionalization

The task of altering the surface properties of a materials to achieve specific binding or adhesion is called sensor or surface functionalization. Here the surface adsorbed layer is called the adlayer. The functionalization adlayer is typically a few nanometers thick, whereas the analyte biomolecules to be detected range from a few nanometers to 15-20 nanometers in diameter or layer thicknesses. Compared to the applied wavelength of nearly 875-1600nm, the molecular size of the analyte is completely subwavelength and does not contribute any scattering or diffraction effects to the guided light. Surface functionalization can be categorized into chemisorption and physisorption processes. They can also be called covalent and non-covalent functionalization respectively as well. The former offers higher

stability and constant surface concentration / attachment throughout the sensing experiment. This type of functionalization is more permanent, as it modifies the surface properties and how the sensor behaves. The latter relies on physisorption, or adhesion to surfaces without a chemical bond. This is less permanent, and not likely to modify the sensor function. The chemisorption method of surface function is more desirable because it provides additional control and reliability.

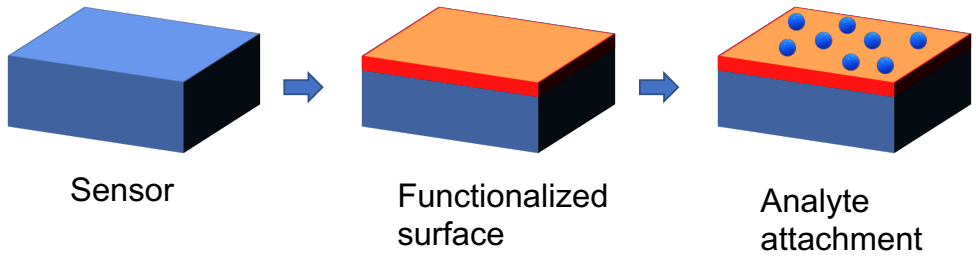

Figure 2. Functionalization of a sensor surface for analyte attachment

To directly attach the targeting molecule to the sensor, a bifunctional linker molecule is generally used. One of end of the linker molecule can attach to the surface of the sensor where the other end has a functional group chosen specifically to bind onto the analyte. In SPR biosensing platforms, the linker often has an alkane with a thiol anchor group to react with the gold surface, while the other end is chosen based on the analyte [14]. For this kind of coating, often a self-assembling monolayer (SAM) is achievable [15].

For silicon biosensors, the surface is often functionalized with light oxidation to create a thin silica layer which binds to specific molecules. The silica surface can be further functionalized with a trichloro, trimethoxy, or a trimethoxy silane group that attaches well with silica [2]. Our waveguide biosensors are functionalized by oxidation, and then further

by 3-aminopropyltriethoxysilane. Our sensor may also be used via physisorption as a reversible process to detect specific liquids / gas.

1.4 Analyte Delivery Methods

Delivery methods are methods used to expose the sensor surface to the analyte. The type of delivery method may be different based on the surface chemistry and bioassay. The delivery method must be economical and chosen is such a way that the exposure amount and duration are optimized. The current methods are droplets, immersion using an open flow cell and a microfluidic flow cell with inlets and outlets with constant analyte flow. Droplets lets the analyte diffuse through the sensing surface which may not be the most efficient method but utilized in our work due to simplicity and minimalistic nature. A microfluidic flow cell can be utilized for our sensor for liquid / gas sensing with physisorption resulting in a sensor that is reversible and re-usable. The delivery methods are illustrated in figure 3.

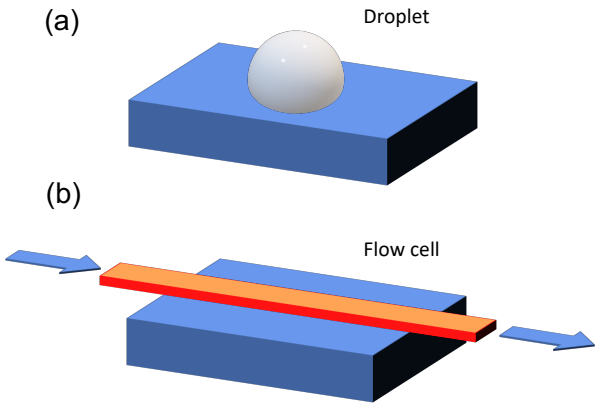

Figure 3. (a) Droplet and (b) flow cell delivery method

1.5 Optical Biosensing Techniques

Optical biosensors operate by generating an optical perturbation caused by the attached analyte. Broadly, they can be divided into two categories: label-based and label-free. In label-based mode, the sensing is performed using a label which then modified the optical signal via colorimetric, luminescent or fluorescent method [13].

The optical biosensing technique can further be divided into two classes. The first platform (which is generally label-based) isolates the optical signal generated by the analyte or the associated label. The most common technique in this category is detecting fluorescence of the analyte molecule [16]. This involves absorption of a photon by the analyte and then subsequently emitting a photon of a different wavelength. Biomolecules that allow this are called fluorophores. Analytes that do not possess this property may be tagged with fluorophores. In the end, the fluorescence signal may be isolated via spectroscopy or optical filters removing background noise. This type of sensors may also work based on absorption may signal detection by measuring the amplitude of light.

1.5.1 Fluorescence based techniques:

A common fluorescence detection technique is the sandwich assay. Here an analyte is bound to a surface using a targeting molecule which is immobilized using previously mentioned chemisorption surface functionalization methods. Then the analyte can be labeled with fluorophores and the fluorescence can be measured to obtain the analyte concentration [17]. One other technique is the total internal reflection fluorescent method [18]. Here, the concentration is measured similarly by the fluorescence given off by the attached labels, but here the fluorophores are excited using the evanescent field from

the total internal reflection beneath the surface. Both techniques are illustrated in figure 4. The drawbacks of such techniques are: 1. The label often interferes with the analyte surface chemistry. High concentration often results in a loss of signal. 2. The fluorescence is qualitative data and quantifying it to a specific concentration is often inaccurate.

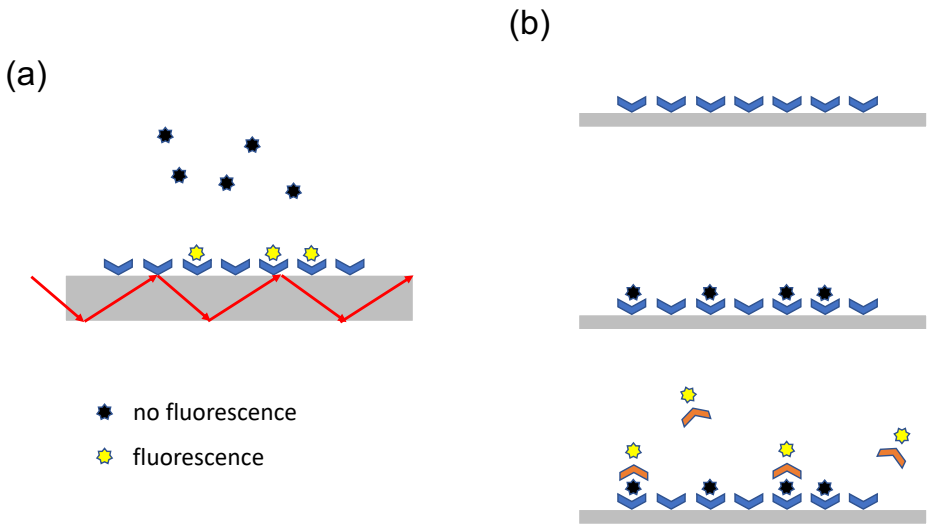

Figure 4. (a) Total internal reflection fluorescence biosensing assay (b) fluorescence-based sandwich assay

The second class of biosensing depends on the phase change of light due to surface analyte attachment. This method requires no labels because it operates based on the local change in refractive index when analytes are bound to the sensor surface. They are generally not limited by the analyte's optical properties and loss generated by previously discussed spectroscopic methods. They are desirable because measuring phase changes is very straightforward in an interferometric configuration. Among these sensing platforms, most prominent are surface plasmon resonance (SPR) [5], guided mode photonic crystals [6], nanophotonic waveguide interferometry [2], whispering gallery resonance [12] and 2D atomic material sensing [10].

1.5.2 Surface Enhanced Raman Spectroscopy (SERS)

This technique increases the vibration spectra of a molecule by several orders of magnitude when near nanoparticles made of gold or silver. The method of operation is shown in figure 5. Applications include a SERS-active surface on the tip of an optical fiber to detect cancer proteins (~100pg) [19]. Literature reports a SERS biosensor designed for protein biomarker detection with an LOD of 5ng l^{-1} [20].

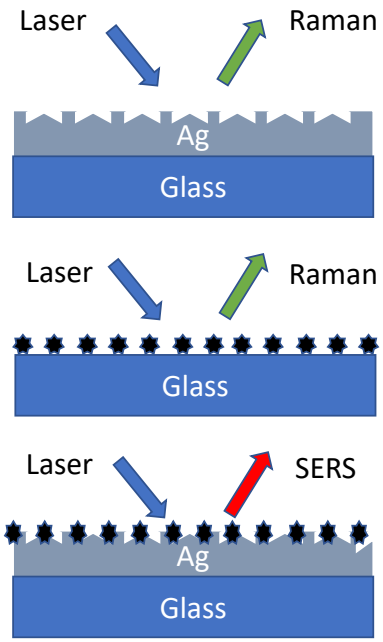

Figure 5. Surface enhanced Raman spectroscopy (SERS) biosensing technique

1.5.3 Surface Plasmon Resonance:

Surface plasmon resonance (SPR) is a label-free phase change optical biosensing technique that has become a benchmark in optical biosensing due to its commercial application in the form of Biacore [21]. Figure 6 shows a typical SPR biosensing setup where a SPR enabled gold-coated glass is surface functionalized. This may represent one wall of a flow cell through which the analyte would flow. Then light is shined on the glass

slide through a prism. At a specific wavelength and angle the SPR conditions would be met and the optical characteristics of the gold coating would change drastically in presence of the target analyte. The information regarding the analyte concentration can be quantified from the modified reflectivity change. The drawbacks associated with SPR are extremely high cost of implementation, bulky form factor and limited LOD [22].

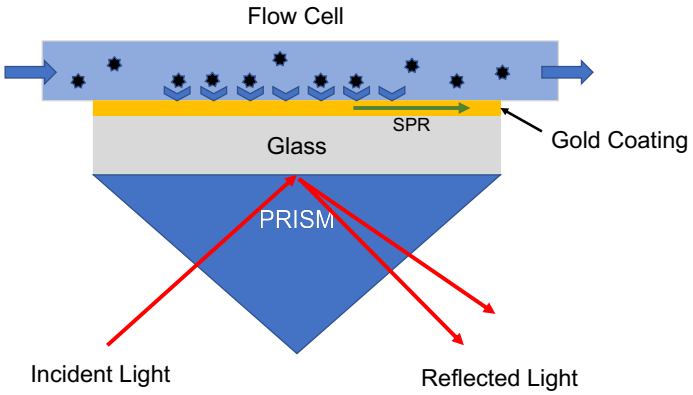

Figure 6. Surface plasmon resonance (SPR) biosensing technique

1.5.4 Whispering gallery resonator (WGM) sensors:

The whispering gallery resonator sensor [23,24] has a similar working principle as the whispering gallery where sound waves take a circular path around a curved wall of a round room. This path is similar to the path the resonant light takes as it circulates the circular cavity. Light at a particular wavelength gets trapped in the circular path which relies on the optical path length ($2\pi rn$; n=refractive index, r = radius) of the ring. This length may be modified by the change in refractive index of the ring brought about by attachment of surface analytes. The resonant wavelength shift corresponds to concentrations of analyte present. The RI perturbation only takes place in the evanescent

field, which drives down the sensitivity for this platform. The working principle is illustrated in figure 7.

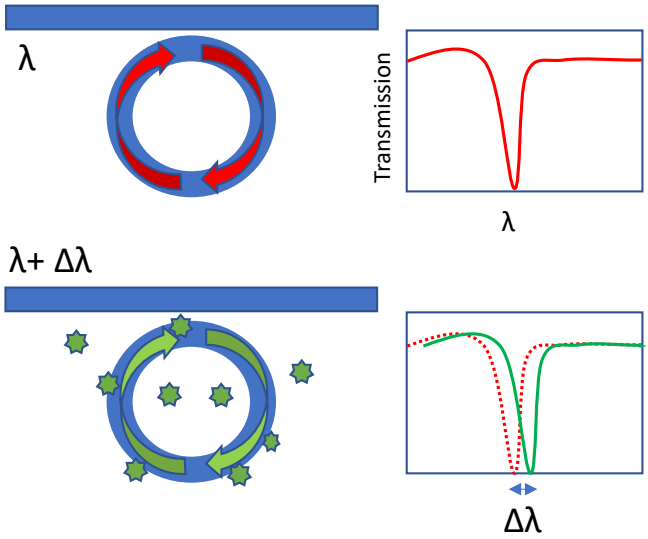

Figure 7. Whispering gallery mode resonator sensor working principle

1.5.5 Other notable techniques

Reflectometric interference spectroscopy is a label-free time-resolved method that relies on white light interference at thin layers. Changes in phase provides information about thickness and refractive index of attached surface analytes. This method was implemented to detect and quantify diclofenac in bovine milk and resolves a LOD of 0.112 $\mu g\ l^{-2}$ [25]. Photonic crystal cavity resonant sensors [26] are another prominent technology to be mentioned. Here, this waveguide is formed by introducing a line defect in a 2D photonic crystal slab.

1.5.6 Optical interferometric waveguide sensors:

Optical interferometric waveguides employ a combination of evanescent field sensing and phase analysis to measure refractive index change. This RI change can then be

corresponded to concentrations of analyte detected. Although common, these evanescent phase sensitive surface adlayer sensors provide very low overlap between the guided mode and the sensing surface. For example, conventional silicon on insulator (SOI) waveguide biosensors achieve a confinement factor of only ~2% in the sensing surface region [7]. The analytes are attached to the outer surface of the waveguide; thus, it can perturb only the evanescent field of the guided mode, which drives down the sensitivity.

1.6 Biosensor Performance Metrics and Requirements

It is important to characterize a biosensor performance and response to analyze the strengths and weaknesses of various sensing platforms. A biosensor should be cost effective, simple to fabricate and characterize and of course, industrially scalable. Our sensors fit into these criteria as discussed later. Sensitivity, selectivity, repeatability, limit of detection (LOD) and dynamic range also comes into play here.

Sensitivity is a key factor in our work and is defined generally as the resonant wavelength shift or refractive index change per molecular adlayer attachment. Details about sensitivity are discussed in chapter 2. Selectivity is the ability of the sensor to perform detection of the target analyte despite presence of other interfering molecules. We achieve this by specific surface chemistry. Repeatability is met when a sensor construction and the experiment is repeatable. This stability may depend on sensor geometry – and may vary based on operating conditions. It is imperative that a sensor meets these criteria.

Limit of detection is the quantity that describes the lowest concentration of analyte the biosensor can detect with a clearly distinguishable signal. The concentration at which the signal to noise ratio is above 1 may be regarded as the LOD. However, experimental

variations should be considered, so this must be confirmed via multiple measurements. Dynamic range of a sensor describes the range of concentration that the sensor can detect accurately before saturating.

An additional metric is biosensor size. Size may determine how the sample may be used in the field. For example, a small size is often preferable because it requires less analytes, can be mass produced at a low cost and can be integrated into medical diagnostic devices.

CHAPTER TWO

MAXIMIZING SENSITIVITY AND CONFINEMENT FACTOR

Refractive index sensing is a label-free biosensing technique that measures the refractive index change of a bulk material due to analyte adsorption. This refractive index change may be complex, and the sensor can be designed to either (1) measure only the real part of the refractive index by change in the resonance conditions or the change of effective index of the guided mode or (2) the imaginary part which would represent the absorption conditions of the biosensor. In any case, it is necessary to both achieve a measurable bulk refractive index shift and a strong overlap between the guided mode and the sensor surface to achieve a significant perturbation in the optical signal.

For RI surface sensing, maximizing sensitivity works two ways: maximizing the bulk refractive index shift and having enough modal overlap to detect all of it. Both methods are discussed in detail in the following sections. Our work focuses mainly on saturating the modal overlap so that the full bulk refractive index shift can be measured.

2.1 Porous Silicon Refractive Index Sensors

Figure 8 (a)-(d) shows the electric field overlap with attached adlayer for TE/TM mode, SPR, slot mode and Bloch surface wave biosensors respectively. The electric field overlap with the surface adlayer is quite limited, and perturbations introduced due to it are small. For example, optimized silicon SOI sensors see only a ~2% modal overlap in the active sensing region [7]. Maximizing sensitivity in these cases is possible by optimizing for a higher evanescent field by pushing the electric field to the cladding region which is undesirable. This limitation can be overcome by introducing porous nanomaterials that

provide high surface area (>100 m^2) and higher modal overlap due to its porous nature (Figure 8(e)-(f)). Porous silicon (pSi) is one such material that was demonstrated as an attractive material due to its high surface area (> 100 m^2 cm^{-3}) and tunable porosity [27–30]. The pores allow bioanalytes to seep through, and the active mode is guided through the porous medium, which surfaces the analytes. This allows a better modal overlap. However, sensitivity is still limited by the modal confinement factor of 40% to 75%, which is available in current pSi strip waveguides.

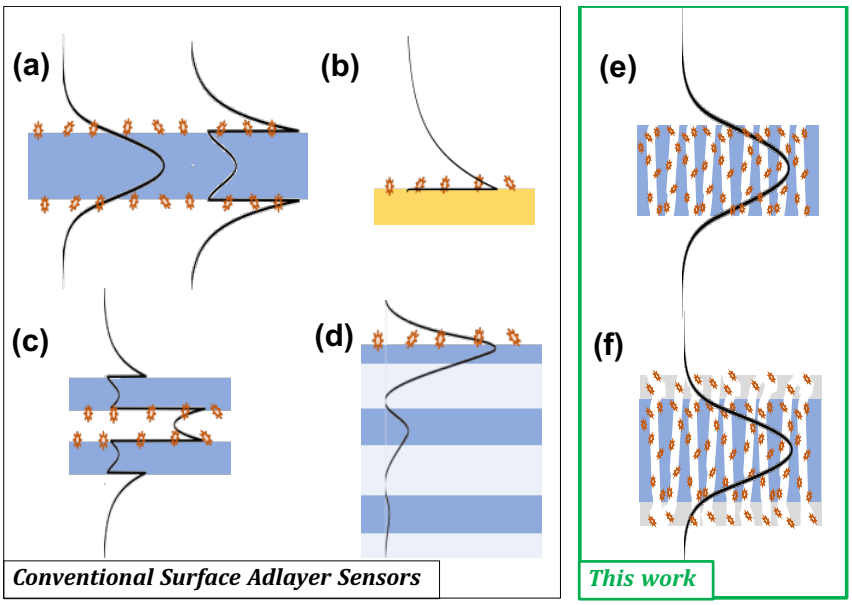

Figure 8. (a) Conventional evanescent surface sensor and (b) pSi surface sensor showing attached small molecules and guided mode

Extending this confinement factor to unity is limited by two things. First, the existent evanescent field around a standard strip waveguide design prevents unity confinement inside the core. This demands a different type of waveguide design. Second, the confinement factor may be increased by increasing the waveguide size, but the waveguide transitions from single mode to multi-mode as size is increased. This is

unattractive particularly for sensing applications based on guided mode. Further, the sensitivity of devices having sub-unity confinement factors are sensitive to fabrication variations that alter the modal confinement. To contend with a robust and scalable platform such as SPR, it is imperative to demonstrate a platform that is not only ultra-sensitive, but also scalable, repeatable and tolerant of critical dimension variations arising from process variation.

Lastly, the current wafer scale fabrication procedure of porous silicon devices requires lithography to be performed on pre-synthesized porous silicon substrates. This requires delicate process optimization, as resists and process chemicals can penetrate through the pores and cause pore clogging, corrosion and contamination [31,32]. This motivates the development of alternative fabrication techniques which minimize fabrication cost and complexity while utilizing the benefits of porous silicon's facile synthesis process and selectable pore size.

In this work, we address above challenges through introducing a novel inverse processing technique where lithography is performed on standard silicon wafer prior to synthesis. We also demonstrate a unique single-mode multi-layer porous silicon rib waveguide design that displays unity confinement factors while retaining single mode operation.

2.2 Maximizing bulk index sensitivity vs. surface adlayer sensitivity

To explore the challenges associated with maximizing sensitivity of a phase sensitive surface adlayer biosensors, we first examine the mathematical definition of

sensitivity. The sensitivity of a waveguide's effective index n_{eff} to perturbation in the refractive index of the waveguide material is defined as:

$$S_1 \equiv \frac{\partial n_{eff}}{\partial n_A} \tag{1}$$

This is derived using first order perturbation theory under the general assumption of high core-cladding index contrast and nonexistent material dispersion [33].

$$S_1 = \frac{n_g}{n_A} \frac{\iint_A \varepsilon |E|^2 dxdy}{\iint_\infty \varepsilon |E|^2 dxdy} = \frac{n_g}{n_A} \Gamma_A \tag{2}$$

Here, n_g is the group index of the guided mode. Γ_A is the transverse confinement factor which is defined by the ratio of the electric field energy inside the sensing region and the total electric field energy. From equation 2, there are a few ways to enhance S_1. One is to fabricate a device with a high group index. Second is to maximize the transverse confinement factor. Achieving a high n_g/n_A ratio means achieving a high electric field energy density which can be achieved by slow light waveguide design, which would also increase the propagation losses. Maximizing the transverse confinement factor is yet an under-explored topic but is a particular focus of our work.

We redefine our sensitivity for our surface adlayer sensor to the waveguide effective index change per change in surface adlayer thickness ($\partial\sigma$) [units: RIU/nm] or effective index change per change in surface adlayer mass surface density [units: $RIUpg^{-1}$ mm^2]. ∂n_A represents refractive index change in the active sensing region, in our case, the porous silicon medium.

$$S_2 \equiv \frac{\partial n_{eff}}{\partial \sigma} = \frac{\partial n_{eff}}{\partial n_A} \frac{\partial n_A}{\partial \sigma} = S_1 \frac{\partial n_A}{\partial \sigma} \tag{3}$$

Here, in the case of bulk index sensors, maximizing S_1 is straightforward as it only requires maximizing mode confinement in the cladding region to drive transverse confinement towards unity. This is achieved by modifying the evanescent nature of the guided mode as shown in surface plasmon-polariton [34], hollow core [35] and guided mode resonance devices [36]. In the case of surface adlayer sensors, increasing the field strength near the waveguide surface increases both the evanescent field strength and the transverse confinement at the cladding. Optimal confinement in the surface (active sensing region) may be achieved by balancing both these trade-offs [7]. For conventional strip waveguide designs, the confinement in the active sensing region where adlayer attachment occurs is on the order of ~ 1%. This can be increased to ~2-5% in the SOI waveguide platform by optimizing TM strip waveguide modes or TE slot waveguide modes [7,37]. These SOI designs demonstrate the benchmark surface sensitivity values of $S_2 = 5x10^{-4}$ [RIU/nm] [7]. In our work, we demonstrate rib waveguide designs that approach sensitivity values of $7x10^{-2}$ [RIU/nm] [2], more than two orders of magnitude higher values compared to the SOI benchmark. Further, we unveil further sensitivity enhancements by tuning the dispersion as a new degree of freedom.

CHAPTER THREE

WAVEGUIDE DESIGN AND FABRICATION

In this chapter we go over the methodologies behind the design of our multi-layer rib waveguide structure. We also propose and demonstrate a new porous silicon processing technique named the "inverse processing technique" which overcomes current porous silicon fabrication and structuring limitations. This novel technique contributes to the unique multi-layer rib type waveguide design we develop and demonstrate in this work.

3.1 Inverse Processing Technique

Our inverse processing technique is shown in Fig. 10 With this technique, silicon wafers may be first patterned using a contemporary patterning technique such as: electron beam lithography or photolithography. Then the patterned wafer is dry etched by reactive ion etching (RIE). This defines the outer dimensions of our waveguides. After patterning, the wafer can be diced into small chips, which then can be used to electrochemically etch into multilayered porous silicon. Wafer scale porous silicon etching is also possible. Anodization is performed on the patterned and diced silicon wafers in 15% ethanoic hydrofluoric acid solution in varying current densities which results in the multilayered structure. This applied current density and duration can precisely control the average porosity, pore dimension, refractive index and layer thicknesses. Similar technique has been previous utilized to create novel micro-optical devices [38].

In this study we model and fabricate both two-layer (2-L) and three-layer (3-L) pSi rib waveguide designs. Silicon etch rate is different at different current densities which can be approximated from available etch rate curves. However, cross section SEM of etched

thin films reveal the etch rate which may be used to calibrate the etch recipe. Refractive index can be measured by fitting the reflectance spectra of the thin film using the transfer matrix method. Here, the film thickness is known from previous SEM measurements. Example of a reflectance spectra fit is given in Fig 9. We choose the core and cladding indices to be 2.1 and 1.56 respectively at λ = 1550nm which require current densities of 4.92mA/cm^2 and 55mA/cm^2 respectively.

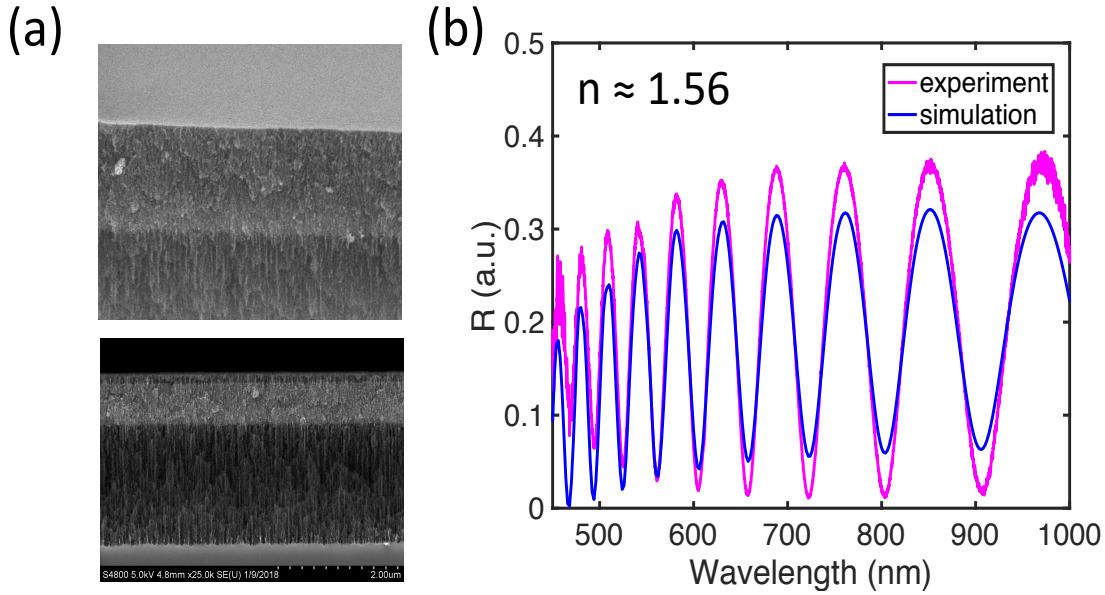

Figure 9. (a) Example cross section SEM images of pSi thin films (b) Reflectance spectra fit using transfer matrix to determine porosity and refractive index at λ = 1550nm

The 2-L design starts with an n = 2.1 index core layer and then an n = 1.56 index cladding layer. The top cladding is air. In the 3-L design, the top air cladding is replaced by a n = 1.56 index pSi layer that can harvest the residual evanescent field. To fabricate this, 55 mA/cm^2 current density is used to create the low index cladding region ($n_{cladding} \approx 1.56$) and 4.92 mA/cm^2 current density for the high index core ($n_{core} \approx 2.1$). The current duration determines the etch depth / layer thickness. For the 2-L waveguides, we

run 4.92 mA/cm^2 for 177 s that creates 800 nm for the core layer and then 55 mA/cm^2 for 70 s that creates 2050 nm for the bottom cladding layer. For the 3-L waveguides, we run 55 mA/cm^2 for 4.5 s for 180 nm top cladding, 4.92 mA/cm^2 for 118s for 650 nm middle core and lastly 55 mA/cm^2 for 77 s for about ~2200 nm bottom cladding. Etched waveguides are oxidized in a furnace at 500°C for 5 minutes to create a thin glass layer for APTES functionalization.

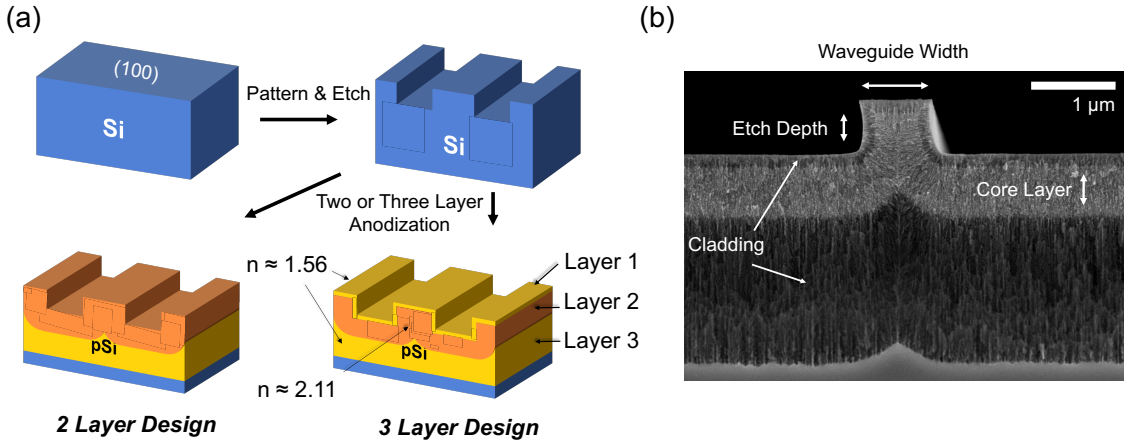

Figure 10. (a) Inverse processing technique demonstrating the pre-patterning of silicon wafers before anodization to fabricate 2-L and 3-L waveguide structures (b) Dimensional parameters for fabricated waveguide structure showing cross sectional scanning electron microscope image. Reprinted from [2].

Figure 11 shows cross-sectional scanning electron microscopy (SEM) images of fabricated 3-L waveguide structures across a width skew. The unique rib type geometry can be seen in this image, which can be solely attributed to our inverse processing technique. The anodization progresses in the <100> direction which is normal to the silicon wafer plane. To keep our waveguides operating in single mode, we choose a width that allows the opposing etch fronts to intersect beneath the rib (Figure 11(d,e)).

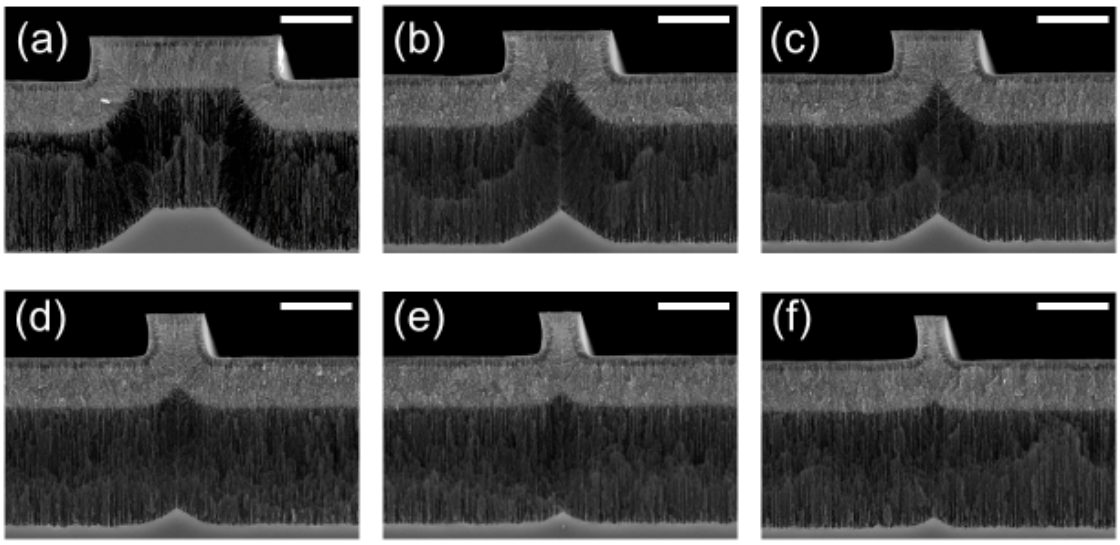

Figure 11. Cross sectional scanning electron microscopy images of fabricated 3-L waveguides after patterning and anodization across a waveguide width skew showing the unique rib type geometry resulting from the inverse processing technique (scale bar = 1 μm). Reprinted from [2].

3.2 Waveguide Design

We create and simulate the unique rib design in a commercial mode solver Lumerical MODE to investigate the confinement factors and surface adlayer sensitivity. We show the confinement factor as a function of waveguide width in Figure 12 for 2-L and 3-L waveguides alongside a conventional pSi strip waveguide. Constant near unity confinement factor is observed for both 2-L and 3-L waveguides across a large width skew. The 2-L waveguide shows higher confinement in the core compared to 3-L waveguides while the 3-L waveguide harvests higher total field, achieving a higher total confinement. The pSi strip waveguide approaches higher modal confinement at the cost of single mode operation. Compared to that, both the 2-L and 3-L rib waveguides retain single mode

operation throughout the large width skew. The pSi strip waveguide shows an overall lower confinement factor compared to the 2-L and 3-L designs.

We also illustrate the sensitivity (S_2) of the pSi strip, 2-L and 3-L waveguide in Figure 12(d-f). We note that due to the smaller pore dimensions of the higher index core layer, it is expected to show ~50-60% larger index shifts, $\partial n_A/\partial\sigma$ from Eq 3, compared to the low index cladding. Thus, the core index is significantly perturbed during sensing, which would cause the multi-mode cut-off to be sensitive to the adlayer thickness. This is showed in Figure 12(d) for a single wavelength (1600 nm). In a practical implementation, it's required to set fabrication parameters so that it ensures single mode operation across large fabrication variations. The 2-L and 3-L designs show single mode operation and a consistent sensitivity across a large dimensional change.

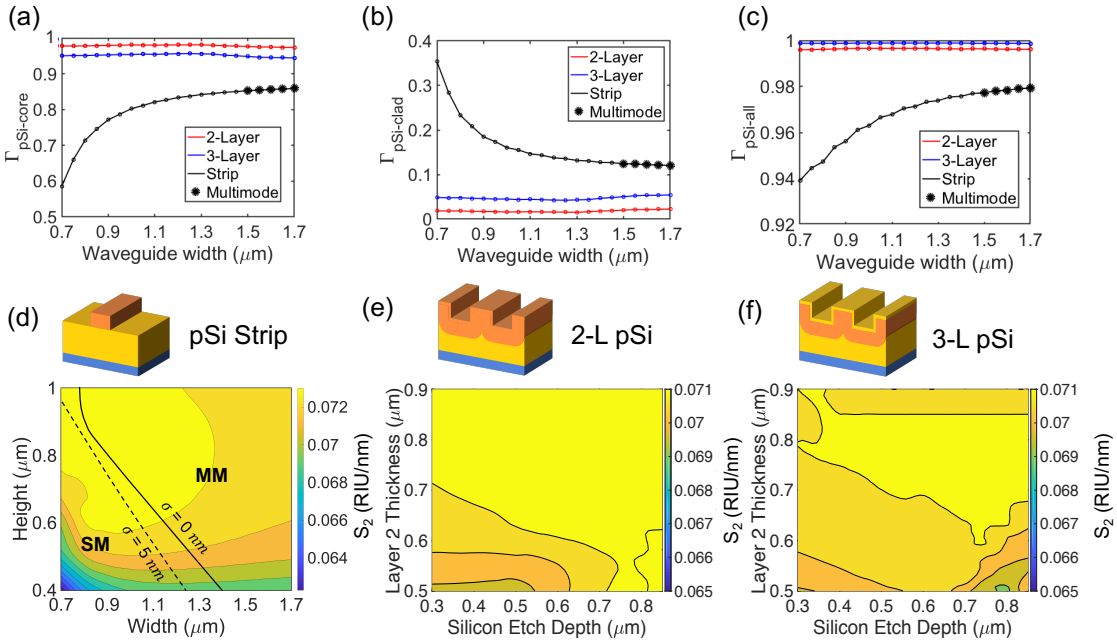

Figure 12. (a) core region, (b) cladding region and (c) total transverse confinement factor vs waveguide width for 2-L, 3L and strip pSi waveguides. (d) pSi strip (e) 2-L and (f) 3-L sensitivity contour vs waveguide dimensions (width = 1μm). Single and multimode boundary is defined in (d). Reprinted from [2].

Our simulated waveguide model is shown in Fig 13. The demonstrated confinement factors are found to be near unity. After experiment, we capture the TE and TM mode shapes (Figure 13(e), 13(f)) on infrared camera (Hamamatsu C2741) and observe them to be identical to the shapes seen in simulation. To ensure single mode operation, we perturb the input coupling fiber and are unable to excite higher order modes.

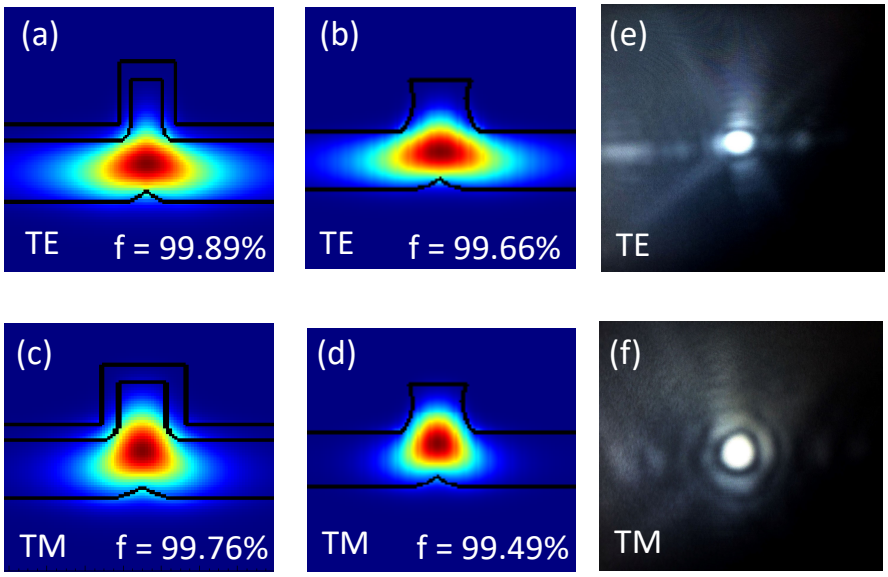

Figure 13. Showing confinement factor and mode shape for simulated (a) TE and (c) TM 3-L waveguides (width =900nm) , (b) TE and (d) TM 2-L (width =900nm) waveguides and (e) TE and (f) TM mode shape captured on IR camera on the 900nm 2-L waveguide. Reprinted from [2].

CHAPTER FOUR

POROUS SILICON WAVEGUIDE INTERFEROMETRY AND SENSING

In this chapter we demonstrate the experimental setup and methods used in the experimental sensing demonstration of our surface adlayer biosensor. The full experiment is performed on both 2-L and 3-L designs and enables characterization of the sensitivity toward surface adlayers. Then the experimentally captured and analyzed data is matched with previously modeled and predicted data and any discrepancy is explained.

4.1 Experimental Setup

Measurements are performed with the waveguide in a Fabry Perot configuration with waveguide length L between the cleaved input and output facets (shown in Figure 14). A near-IR tunable laser (Santec TSL-510) with wavelength sweep functionalities from 1560-1680 nm is used at the input facet. We capture the output spectrum using a photodetector (Newport 918D-IR-OD3R) coupled to a power meter (Newport 2936-R) at the output facet. An infrared camera (Hamamatsu C2741) is used interchangeably at the output facet for imaging and to ensure proper coupling and single mode operation (Figure 14). We also have the option to use a polarizer in the output facet to identify and tune in to the desired TE/TM mode using a manual polarization controller. An example spectrum captured from a 2-L waveguide is shown in figure 14(b). Running a fast Fourier transform (FFT) on the captured spectra shows a peak in the frequency domain which equals the value $2n_gL$ (Figure 14(c)). Here, n_g is the group index of the guided mode and L is the length of the

Fabry Perot cavity. Figure 14(c) shows FFT peak plotted on the same scale for TE and TM modes.

Our approach is similar to pSi thin film biosensors where taking the FFT of an optical reflection spectrum produces a single peak which corresponds to the total optical path length ($2n_gL$) of the Fabry-Perot cavity [34,35]. This approach attractively enables sensing to be performed without tracking a specific spectral feature or resonance shift. We also note that owing to the significantly enhanced ~mm scale path length of our devices, i.e. versus the ~μm path length of pSi thin film devices, the interferometric resolution and limit of detection is correspondingly enhanced. This principle is experimentally supported by the ultra-narrow FFT peaks we are able resolve in the Fourier domain, where the peak $2n_gL$ value normalized to the full width half maximum, $\Delta 2n_gL$, is observed to be ~150 in our ~1 mm length interferometers when analyzed over a spectral bandwidth of ~100 nm versus a value $2n_gL/\Delta 2n_gL$ ~5 in typical micro-scale thin-film pSi biosensors, typically analyzed over a ~500 nm bandwidth [39].

Throughout our all of our experiments we observe a birefringence between TE and TM polarization of approximately $\Delta n_g \sim 0.15$ RIU. We attribute this to two primary factors: (1) the anisotropic refractive index nature of porous silicon and (2) waveguide dispersion. From simulations assuming a homogenous porous silicon material with no anisotropy, only a modest $\Delta n = 0.03$ RIU is predicted from modal dispersion. Hence the dominant source of birefringence between TE and TM polarization is attributed to the strong anisotropy of the porous silicon. We note that the $\Delta n_g \sim 0.15$ observed in our work is comparable to the

birefringence observed in previous works concerning porous silicon thin films at 55% porosity [40,41].

Our Fabry Perot measurement technique also allows us to measure the waveguide propagation loss, which is estimated here to be 2.7 ± 0.3 dB/mm. Loss characterization is performed by analyzing the measured fringe contrast and assuming facet reflectivities,

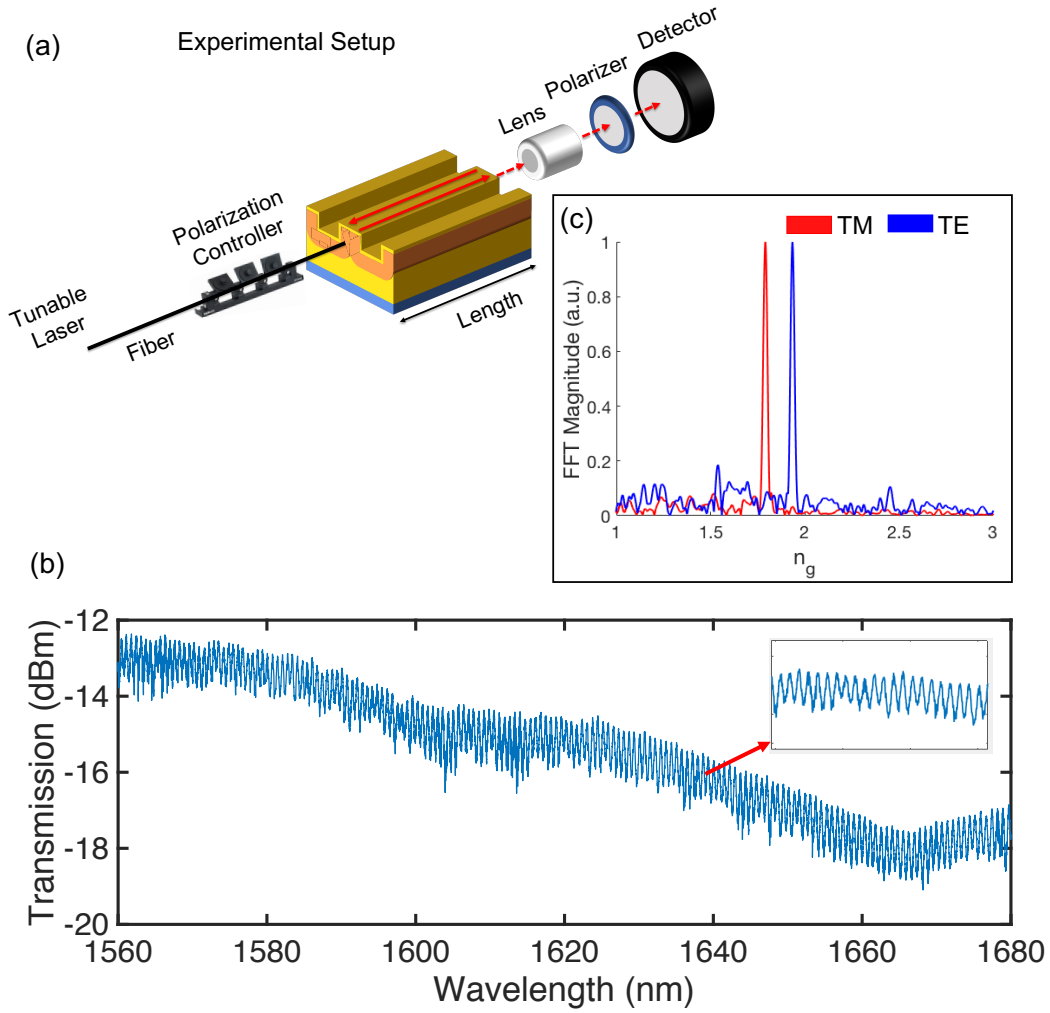

Figure 14. (a) Experimental setup of the Fabry-Perot configuration (b) Spectrum sweep captured from 1560-1680 nm wavelength sweep of the 900nm 2-L waveguide (c) FFT analysis shows peaks representing n_g. A polarizer is used to recognize the TE and TM peaks. Reprinted from [2].

$R_1 = R_2 = 0.11$, which are calculated using Fresnel coefficients. Our measured loss agrees with loss measured in recent porous silicon waveguides [27]. We note that, imperfect

cleave angles can perturb the fringe contrast which may lead to an overestimation of the waveguide losses. These losses can be attributed to free carrier absorption in highly doped silicon and Rayleigh scattering from surface scattering and disorder.

To measure the waveguide sensitivity to surface adlayer attachments, we use a silane molecule named 3-aminopropyltriethoxysilane (3-APTES), which is commonly used to functionalize silica surfaces for organic molecule attachments. The 3-APTES monolayer corresponds to a 0.8 nm thick surface adlayer with a refractive index near ~1.46 RIU [42]. To enable 3-APTES attachment, the pSi waveguides are oxidized for 5 minutes at 500 °C to form a glass surface.

After oxidation, the modified spectra of pSi waveguides are measured again for reference. The waveguides are then exposed to 4% 3-APTES in a 1:1 mixture of deionized water and methanol for approximately 45 minutes. Then the samples are rinsed with water and dried under air flow. The final transmission spectra are recorded after this step, and the group index is measured and plotted via FFT method.

4.2 Surface Sensing Characterization

Figure 15(a) and 15(b) show the cross-section SEM images of 2-L waveguides having 900nm and 500nm width at the base respectively. Transmission spectra were collected under both TE and TM polarization and the corresponding FFT peaks representing the group index are presented. Figure 15(c) and 15(d) represent only the TE FFT peaks from spectra captured from 15(a) and 15(b) respectively.

The measured group indices shown have a clear shift after oxidation and silanization. This group index reduction due to oxidation is $\Delta n_g \approx 0.105$ and the increase

due to 3-APTES attachment is $\Delta n_g \approx 0.058$. Considering a 3-APTES monolayer that corresponds to a 0.8 nm thickness adlayer [], the resultant surface adlayer sensitivity is $\partial n/\partial \sigma \approx 0.0725$ RIU/nm. This result agrees with our simulated effective index sensitivity S_2 (~0.07 RIU/nm, Figure 3(d)).

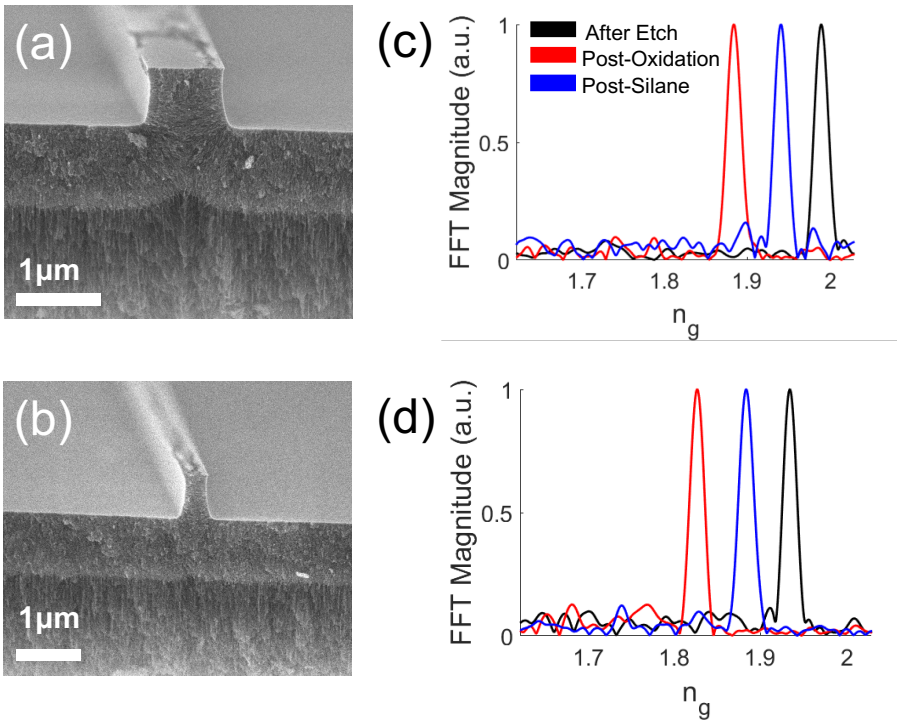

Figure 15. (a) Cross sectional SEM of 2-L waveguides with (a) 900 nm and (b) 500 nm width at base. (c) Group index peaks for 900 nm and (d) 500 nm waveguide. Reprinted from [2].

A constant Δn_g observed for both narrow and wide waveguides which confirms our expectations that the sensitivity is not a function of waveguide dimensional parameters (Figure 12). This consistency of Δn_g also verifies the repeatability of the process. This tolerance to critical dimensions is a significant improvement over SOI sensors that show both a much lower sensitivity and a much higher variation over dimensional variation (i.e. 20% S_2 variation for 150nm width variation) [7].

We further experiment with 3-L designs which have an additional low index cladding layer (thickness ≈ 180nm) on top of the core (Figure 10(b)). Figure 16 shows the above experiment results for 3-L waveguides. Here the group index reduction ($\Delta n_g \approx 0.25$) due to oxidation is ~150% larger compared to the 2-L waveguides. Similarly, an enhanced response is observed also for the 3-APTES attachment where $\Delta n_g \approx 0.0.078$ which corresponds to a surface adlayer sensitivity of $\partial n/\partial \sigma \approx 0.0975$ RIU/nm (assuming nominal 0.8 nm monolayer), which is 40% larger than both the 2-L and the predicted 3-L sensitivity. This sensitivity exceeds the effective medium sensitivity of the higher sensitivity core layer which we model to be ~0.074 RIU/nm for an average ~15 nm pore diameter and ~55% porosity [42].

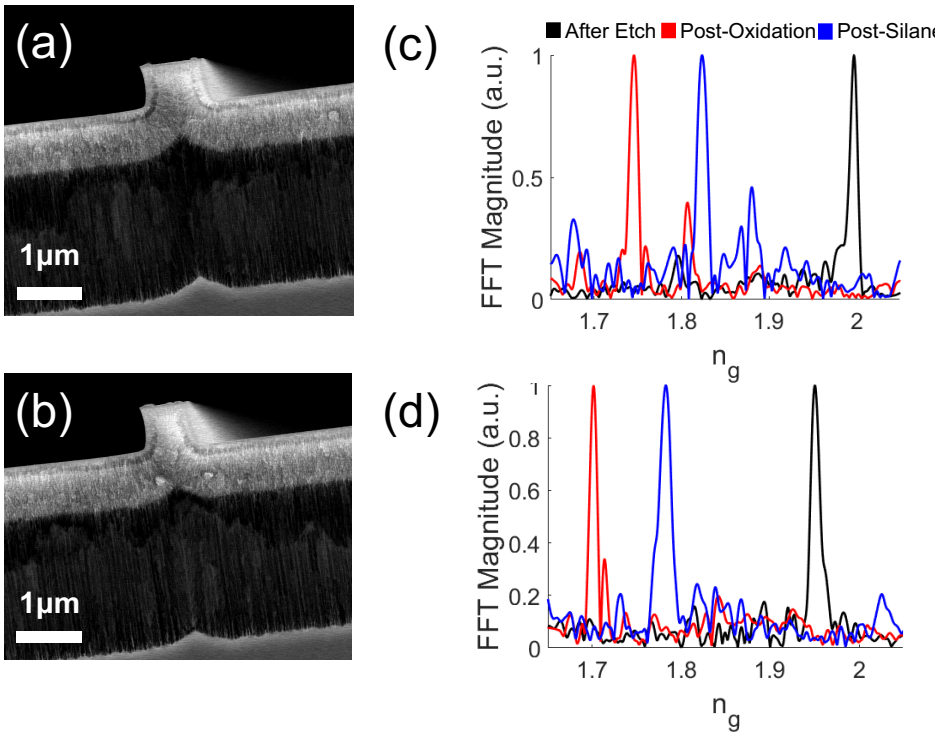

Figure 16. (a) Cross sectional SEM of 3-L waveguides with (a) 700 nm and (b) 600 nm width at base. (c) Group index peaks for 700 nm and (d) 600 nm waveguide. Reprinted from [2].

4.3 Exceeding the sensitivity of bulk pSi: The Dispersion Degree of Freedom

In our 3-L waveguide measurements, we notice an unexpectedly enhanced sensitivity response – which we refer to as "sensitivity dispersion". The simulated waveguide sensitivity is based on the change in waveguide effective index $\partial n_{eff}/\partial\sigma$. However, our experiment setup measures the group index n_g and its perturbation $\partial n_g/\partial\sigma$, which is expressed by:

$$n_g = n_{eff} - \lambda\left(\frac{\partial n_{eff}}{\partial\lambda}\right) \tag{4}$$

$$\frac{\partial n_g}{\partial\sigma} = \frac{\partial n_{eff}}{\partial\sigma} - \frac{\partial}{\partial\sigma}\left(\frac{\partial n_{eff}}{\partial\lambda}\right)\lambda \tag{5}$$

From Eq 5 and 3, we can derive the group index sensitivity in terms of effective index sensitivity S_2:

$$S_3 \equiv \frac{\partial n_g}{\partial\sigma} = S_2 - \lambda\frac{\partial S_2}{\partial\lambda} \tag{6}$$

This confirms that the change in group index is equal to the change in effective index only when dispersion is non-existent across the wavelength sweep, i.e. $\frac{\partial}{\partial\sigma}\left(\partial n_{eff}/\partial\lambda\right)\lambda = 0$ or the phase sensitivity is constant across wavelength such as $\frac{\partial S_2}{\partial\lambda} = 0$. The observed enhanced sensitivity thus can be attributed to a non-negligible value of the sensitivity dispersion. This also suggests that S_2 is larger at shorter wavelengths.

The usage of thin cladding layers that modify the evanescent region of guided modes have been previous demonstrated to change confinement hence introduce dispersion [43–45]. Here, our data shows a clear dispersion effect in our 3-L waveguide

sensors. This effect is unlikely to take place in traditional evanescent sensors because they have decaying confinement in shorter wavelengths, and the modal dispersion is dominated by bulk material order and symmetry – which has negligible presence in the active sensing region. In our 3-L device, the material property modulation (refractive index) due to adlayer attachment is different in the core and cladding regions, approximately $\Delta n \approx 0.05$, which demonstrates a different sensitivity due to different porosity and pore diameter in each layer [42] .

Mode calculations of 3-L devices confirm that group index shift can be indeed larger than effective index shift when each layer demonstrates different sensitivity values. A proof of concept simulation is shown in Figure 8 where cladding and core layers are assumed to have a refractive index shift Δn of 0.02 and 0.1 respectively due to adlayer attachment. As seen, the group index change exceeds the effective index change here when top cladding: core ratio is 1 (fraction = 0.6). We note that this simulation ignores the anisotropic nature of porous silicon and material dispersion, but future work exploring this effect with anisotropic and dispersive materials may give us more insight into this phenomenon. This would require modelling of both a dispersive porous silicon bulk material and an anisotropic refractive index matrix. We note that the oxidation and silanization step would also modify the anisotropy and have an effect on the total group index shift (n_g).

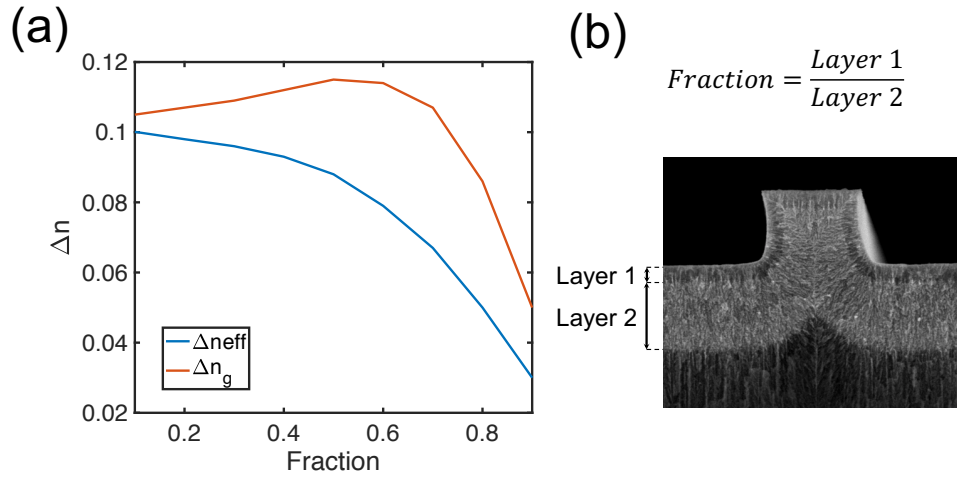

Figure 17. (a) Effective index and group index shift due to adlayer attachment with $\Delta n_{cladding} = 0.02$ RIU and $\Delta n_{core} = 0.1$ RIU (b) Showing the definition of fraction and layer 1 and layer 2 thicknesses on a cross sectional SEM image

Assuming sensitivity dispersion as the major contributor in the enhanced sensitivity response, we calculate the 3-L waveguide dispersion to be $\frac{\delta}{\delta\sigma}\left(\frac{dn_{eff}}{d\lambda}\right) \approx 1.56 \times 10^{-5} \frac{RIU}{nm} nm^{-1}$ at λ = 1600 nm. We suggest from this observation that the sensitivity may be further enhanced by tailoring the layer parameters to enhance the waveguide dispersion.

4.4 Data summary

The measured group index shifts from the experimental data are summarized in Table 1:

Table 4.1 Summary of measured changes in group index (Δn_g) from oxidation and silane attachment.

Waveguide Type	Width	Δn_g(ox)	Δn_g(silane)	Δn_g(ox)/n_g	Δn_g(sil)/n_g(ox)
2-L	900 nm	0.105	0.057	0.052	0.030
	500 nm	0.109	0.059	0.056	0.032
3-L	700 nm	0.249	0.082	0.127	0.048
	600 nm	0.252	0.078	0.126	0.044

Figure 18 shows modeled refractive index shift and measured group index shift respectively for 2-L and 3-L waveguides alongside modeled and measured effective index change of SOI waveguides to small molecule adlayer attachments. We observe more than 100x higher sensitivity values for both modeled and measured 2-L and 3-L waveguides compared to contemporary evanescent SOI sensors [7]. We note that both 2-L and 3-L experimental values show higher sensitivities compared to modeled sensitivity values. The 3-L waveguides show higher sensitivity due to dispersion effects that are explained before.

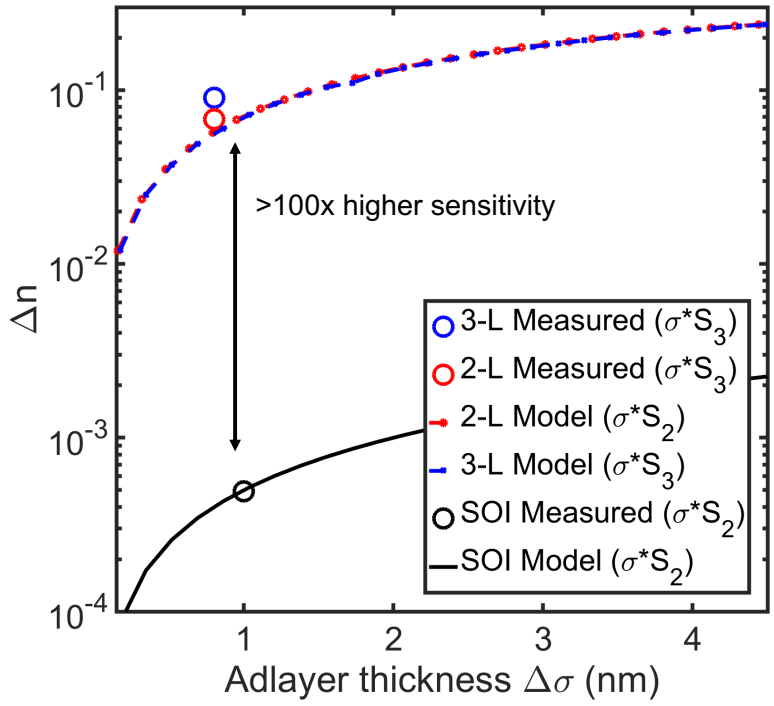

Figure 18. Modeled and measured data of waveguide effective (group) index change σS_2 (S_3) vs. adlayer thickness of 2-L and 3-L pSi waveguides and optimized SOI waveguides from [7]. Reprinted from [2].

CHAPTER FIVE

CONCLUSION AND OUTLOOK

5.1 Conclusion

We demonstrated the design, fabrication and characterization of a unity confinement factor porous silicon rib waveguide that demonstrates record level surface adlayer sensitivity $S_2 \sim 0.08$ RIU/nm. We achieve sensitivity values that surpass optimized evanescent SOI sensors ($S_2 \sim 0.0005$ RIU/nm [7]) by two orders of magnitude and shows comparable performance (S ~ 60-90 nm/nm) to commercialized SPR sensors (S ~1.8 nm/nm [46]) but at a competitive and very compact configuration.

One other key factor is our waveguide's capability for retaining single mode characteristics over a large dimensional variation. This provides great flexibility as our sensor is operational independent of process variation. Nominal confinement factors near ~99% is achievable in both 2-layer and 3-layer waveguides which is able to measure the entire refractive index shift in the bulk pSi material. For the 3-layer material, we observe enhanced response in our experimental measurements. We posit that the top cladding layer is the primary contributor to this enhanced response and model a dispersive birefringent model to confirm our theory. This allows us to measure shifts greater than the bulk RI shift which allows very low LOD to be achieved.

We also demonstrate an inverse processing technique, where anodization on pre-patterned wafers are performed to overcome porous silicon wafer fabrication limitations and achieve unique birefringent devices.

5.2 Outlook

For the first time, we demonstrate a waveguide with near unity confinement factor in the sensing region. This allows fabrication of future ultra-sensitive whispering gallery resonators, 1-D photonic crystals such as Bragg mirrors, and also beam steering devices for sensing purposes. Compared to current WGM biosensors with less than 1% modal overlap, we can expect a few orders of magnitude higher sensitivity in our pSi WGM configuration. This also applies to photonic crystal cavities. The beam steering approach can be sensitive enough to function as a binary detection device. Devices made in our approach will have very low LOD owing to the maximal modal overlap while being field-compatible due to its small form factor and ease of use. Because of tunable pore size and available library of surface chemistry, our sensor can be utilized to detect analytes ranging from specific gas particles such as methane and aerosol, environmental food and water-borne toxins to DNA aptamers and protein. Aptamers can target specific toxins and can be engineered to detect heavy metal ions as well. Also, non-specific surface attachments invalidate the evanescent field sensors' performance. In our case, the unity confinement in the waveguide renders the effects of non-specific surface attachments negligible. However, there exists several key challenges regarding our waveguide sensor:

- Porous silicon waveguide platform is lossy which would impact the length of the chip and thus the LOD. These losses arise from Rayleigh scattering and free carrier absorption. As future work, we propose full oxidation of the sensor which would lead to a lower index contrast and reduction of free carrier absorption losses. Porous

silica has seen to have losses as low as ~0.06 dB/cm [47]. This would allow us to realize longer path lengths resulting in a lower LOD and higher Q factor.

- Conversion to porous silica would reduce the refractive and the group index (n_g) of the waveguide which decreases the sensitivity. This may result in a leaky waveguide that has trouble guiding a mode. Rigorous characterization of current density and associated refractive index mapping is required to create structures capable of guiding modes.
- Volume expansion resulting from the conversion from Si to SiO_2 would result in pore shrinkage, and in < 50% porosity cases, will result in closed pores. This is critical as analyte infiltration is key in our sensing approach. This can be solved by starting with a > 50% porosity.
- If extremely high porosity layers (>75%) are chosen throughout the device structure, it may be an unstable porous silicon skeleton prone to breakdown. Oxidation causes further film stress ending up being a structurally unstable sensor.

Some ways around these limitations are:

1. Optimizing a standard recipe for etch and oxidation,
2. Increasing average refractive index of porosified silica by depositing a thin layer of an external high index material to increase the index contrast

One other minor limitation is the device reusability – which may be solved using phosphate buffered saline which causes deterioration of the silica layer [48]. Direct physisorption-based monitoring is also implementable with our sensors in a flow cell for gas or liquid analyte detection.

APPENDIX

Appendix A

Experimental Section

Patterning: The GDSII pattern file is first created using open source software Klayout. The GDSII file can then be converted to JEOL compatible *.v30 files to be written / patterned on the wafer. 4-inch (100) p-type silicon wafers (0.01 Ω-cm) are first coated with electron beam resist ZEP520A and spun in 3000RPM for 45 seconds to have a thin layer of electron beam resist. Then electron beam lithography (JEOL JBX-9300FS) is performed on the wafer with a base dose of 300 and shot pitch of A4. After exposure the wafers are developed in Xylene for 30 seconds. After that reactive ion etching (Oxford Plasmalab-1000) is performed on the developed resist. Here, standard Si waveguide etch recipe (C_4F_8 – 27 sccm, SF_6 – 12 sccm, Ar – 2 sccm) is used for 5 minutes. This results in a silicon etch depth of ~650 nm. Silicon ribs ranging from 0.3 to 2.5 microns are fabricated for testing.

Porous silicon etching: The silicon wafer is diced into ~2 x ~2 inch dies. An electrochemical cell with a platinum cathode can be used as the etch cell. 15% ethanoic hydrofluoric acid is poured in the etch cell where the silicon die works as the anode. A Keithley DC etch system is used as the current source.

Numerical Modeling: Waveguide modeling is done in a commercial eigenmode solver (Lumerical MODE Solutions). Simulations are performed at a wavelength of 1600nm. Porous silicon model is established using Bruggeman effective medium approximation.

Here an average pore diameter of ~15nm and ~35nm is assumed for the core and cladding layer respectively []. Here, we ignore the anisotropic and dispersive nature of porous silicon. Here, a more robust approach would be to employ a spatially varying permittivity tensor or import a dispersive material model to represent the porous silicon structure.

Optical Measurements: In the input, a near-IR tunable laser (Santec TSL-510). It can perform wavelength sweep from 1560 nm to 1680 nm. At the output, a photodetector (Newport 918D-IR-OD3R) is coupled to a power meter (Newport 2936-R). An infrared camera (Hamamatsu c2741) can be used at the output facet for imaging (Fig. 13e, 13f). We also use a polarizer at the output facet to detect TE or TM polarization modes that we excite using a manual polarization controller. The captured spectrum is saved in a text file and then may be analyzed by running a fast Fourier transform in MATLAB/Python where the x axis of the peak corresponds to the total path length $2n_gL$ where n_g is the group index and L is the length of the Fabry-Perot cavity [49].

REFERENCES

1. D. R. Thevenot, K. Toth, R. A. Durst, and G. S. Wilson, "Technical report Electrochemical biosensors : recommended definitions and classification," **16**, 121–131 (2001).
2. Tahmid H. Talukdar, Gabriel D. Allen, Ivan Kravchenko, and Judson D. Ryckman, "Single-mode porous silicon waveguide interferometers with unity confinement factors for ultra-sensitive surface adlayer sensing," **27**, 22485–22498 (2019).
3. I. Koh and L. Josephson, "Magnetic Nanoparticle Sensors," 8130–8145 (2009).
4. J. M. Perez, L. Josephson, T. O. Loughlin, D. Högemann, and R. Weissleder, "Magnetic relaxation switches capable of sensing molecular interactions," **20**, (2002).
5. X. H. Wang and S. Wang, "Sensors and biosensors for the determination of small molecule biological toxins," Sensors **8**, 6045–6054 (2008).
6. Y. Zhuo and B. T. Cunningham, "Label-free biosensor imaging on photonic crystal surfaces," Sensors (Switzerland) **15**, 21613–21635 (2015).
7. S. TalebiFard, S. Schmidt, W. Shi, W. Wu, N. A. F. Jaeger, E. Kwok, D. M. Ratner, and L. Chrostowski, "Optimized sensitivity of Silicon-on-Insulator (SOI) strip waveguide resonator sensor," Biomed. Opt. Express **8**, 500 (2017).
8. M. Iqbal, M. A. Gleeson, B. Spaugh, F. Tybor, W. G. Gunn, M. Hochberg, T. Baehr-Jones, R. C. Bailey, and L. C. Gunn, "Label-Free Biosensor Arrays Based

on Silicon Ring Resonators and High-Speed Optical Scanning Instrumentation," IEEE J. Sel. Top. Quantum Electron. **16**, 654 (2010).

9. C. C. Evans, C. Liu, and J. Suntivich, "TiO2 nanophotonic sensors for efficient integrated evanescent-Raman spectroscopy," ACS Photonics acsphotonics.6b00314 (2016).
10. D. Rodrigo, O. Limaj, D. Janner, D. Etezadi, F. J. García De Abajo, V. Pruneri, and H. Altug, "Mid-infrared plasmonic biosensing with graphene," Science (80-.). **349**, 165–168 (2015).
11. A. Leung, P. M. Shankar, and R. Mutharasan, "A review of fiber-optic biosensors," **125**, 688–703 (2007).
12. T. Yoshie, L. Tang, and S. Y. Su, "Optical microcavity: sensing down to single molecules and atoms," Sensors **11**, 1972 (2011).
13. P. Damborsky, J. Svitel, and J. Katrl, "Optical biosensors," 91–100 (2016).
14. E. G. Gauglitz, *Handbook of Spectroscopy Near-Infrared Spectroscopy Handbook of Analytical Techniques In-Situ Spectroscopy in Heterogeneous Catalysis* (2003).
15. N. K. Chaki and K. Vijayamohanan, "Self-assembled monolayers as a tunable platform for biosensor applications," **17**, 1–12 (2002).
16. M. Strianese, M. Staiano, G. Ruggiero, T. Labella, C. Pellecchia, and S. D. Auria, "Fluorescence-Based Biosensors," **875**, (n.d.).
17. K. Girigoswami and N. Akhtar, "Nanobiosensors and fluorescence based biosensors : An overview," **10**, 1–17 (2019).
18. K. N. Fish, "Total Internal Reflection Fluorescence (TIRF) Microscopy," 1–13

(2009).

19. K. W. Kho, U. S. Dinish, A. Kumar, and M. Olivo, "Frequency Shifts in SERS for Biosensing," 4892–4902 (2012).

20. S. K. Srivastava, A. Shalabney, I. Khalaila, and C. Grüner, "SERS Biosensor Using Metallic Nano-Sculptured Compound Biomarker Vitellogenin," 1–9 (2014).

21. D. G. Myszka, X. He, M. Dembo, T. A. Morton, and B. Goldstein, "Extending the Range of Rate Constants Available from BIACORE : Interpreting Mass Transport-Influenced Binding Data," Biophys. J. **75**, 583–594 (1998).

22. H. H. Nguyen, J. Park, S. Kang, and M. Kim, "Surface Plasmon Resonance: A Versatile Technique for Biosensor Applications," 10481–10510 (2015).

23. X. Jiang, A. J. Qavi, S. H. Huang, and L. Yang, "Whispering gallery microsensors : a review," (2002).

24. S. H. Huang, S. Sheth, E. Jain, X. Jiang, S. P. Zustiak, and L. Yang, "Whispering gallery mode resonator sensor for in situ measurements of hydrogel gelation," **26**, 788–795 (2018).

25. S. Rau, U. Hilbig, and G. Gauglitz, "Label-free optical biosensor for detection and quantification of the non-steroidal anti-inflammatory drug diclofenac in milk without any sample pretreatment," 3377–3386 (2014).

26. G. A. Rodriguez, P. Markov, A. P. Cartwright, M. H. Choudhury, F. O. Afzal, T. Cao, S. I. Halimi, S. T. Retterer, I. I. Kravchenko, and S. M. Weiss, "Photonic crystal nanobeam biosensors based on porous silicon," Opt. Express **27**, 9536 (2019).

27. G. A. Rodriguez, S. Hu, and S. M. Weiss, "Porous silicon ring resonator for compact, high sensitivity biosensing applications," Opt. Express **23**, 7111 (2015).

28. R. Caroselli, S. Ponce-Alcántara, F. P. Quilez, D. M. Sánchez, L. T. Morán, A. G. Barres, L. Bellieres, H. Bandarenka, K. Girel, V. Bondarenko, and J. García-Rupérez, "Experimental study of the sensitivity of a porous silicon ring resonator sensor using continuous in-flow measurements," Opt. Express **25**, 31651–31659 (2017).

29. P. Azuelos, P. Girault, N. Lorrain, and Y. Dumeige, "Optimization of porous silicon waveguide design for micro-ring resonator sensing applications," J. Opt. **20**, 1–13 (2018).

30. S. Mariani, V. Robbiano, L. M. Strambini, A. Debrassi, G. Egri, L. Dähne, and G. Barillaro, "Layer-by-layer biofunctionalization of nanostructured porous silicon for high-sensitivity and high-selectivity label-free affinity biosensing," Nat. Commun. **9**, (2018).

31. J. D. Ryckman, M. Liscidini, J. E. Sipe, and S. M. Weiss, "Direct imprinting of porous substrates: A rapid and low-cost approach for patterning porous nanomaterials," Nano Lett. **11**, (2011).

32. D. J. Sirbuly, G. M. Lowman, B. Scott, G. D. Stucky, and S. K. Buratto, "Patterned microstructures of porous silicon by dry-removal soft lithography," Adv. Mater. **15**, 149–152 (2003).

33. J. T. Robinson, K. Preston, O. Painter, and M. Lipson, "First-principle derivation of gain in high-index- contrast waveguides," Opt. Express **16**, 16659–16669

(2008).

34. T. Chung, S. Y. Lee, E. Y. Song, H. Chun, and B. Lee, "Plasmonic nanostructures for nano-scale bio-sensing," Sensors **11**, 10907–10929 (2011).

35. G. Testa, G. Persichetti, and R. Bernini, "Liquid core ARROW waveguides: A promising photonic structure for integrated optofluidic microsensors," Micromachines **7**, (2016).

36. Y. Wan, N. A. Krueger, C. R. Ocier, P. Su, P. V Braun, and B. T. Cunningham, "Resonant Mode Engineering of Photonic Crystal Sensors Clad with Ultralow Refractive Index Porous Silicon Dioxide," Adv. Opt. Mater. **5**, 1–7 (2017).

37. F. Dell'Olio and V. M. N. Passaro, "Optical sensing by optimized silicon slot waveguides," Opt. Express **15**, 4977 (2007).

38. N. A. Krueger, A. L. Holsteen, S. Kang, C. R. Ocier, W. Zhou, G. Mensing, J. A. Rogers, M. L. Brongersma, and P. V Braun, "Porous Silicon Gradient Refractive Index Micro-Optics," (2016).

39. M. M. Orosco, C. Pacholski, and M. J. Sailor, "Real-time monitoring of enzyme activity in a mesoporous silicon double layer," Nat. Nanotechnol. **4**, 255–258 (2009).

40. J. Álvarez, P. Bettotti, I. Suárez, N. Kumar, D. Hill, L. Pavesi, and J. Martínez-pastor, "Birefringent porous silicon membranes for optical sensing," Opt. Express **19**, 26106–26116 (2011).

41. N. Ishikura, M. Fujii, K. Nishida, S. Hayashi, and J. Diener, "Dichroic rugate filters based on birefringent porous silicon Abstract :," Opt. Express **16**, 5091–

5094 (2008).

42. H. Ouyang, C. C. Striemer, and P. M. Fauchet, "Quantitative analysis of the sensitivity of porous silicon optical biosensors," Appl. Phys. Lett. **88**, 1–4 (2006).

43. J. Guo, Y. Liang, and X. G. Huang, "Pure Dielectric Waveguides Enable Compact, Ultrabroadband Wave Plates," (2016).

44. S. Jahani, S. Kim, J. Atkinson, J. C. Wirth, F. Kalhor, A. Al Noman, W. D. Newman, P. Shekhar, K. Han, V. Van, R. G. Decorby, L. Chrostowski, M. Qi, and Z. Jacob, "Controlling evanescent waves using silicon photonic all-dielectric metamaterials for dense integration," Nat. Commun. **9**, 1–9 (2018).

45. S. Jahani and Z. Jacob, "Transparent subdiffraction optics : nanoscale light confinement without metal," Optica **1**, 96–100 (2014).

46. F. Dell'Olio, D. Conteduca, M. De Palo, and C. Ciminelli, "Design of a New Ultracompact Resonant Plasmonic Multi-Analyte Label-Free Biosensing Platform," 1–17 (2017).

47. D. Duchesne, M. Ferrera, L. Razzari, R. Morandotti, B. E. Little, S. T. Chu, and D. J. Moss, "Efficient self-phase modulation in low loss , high index doped silica glass integrated waveguides," **17**, 1865–1870 (2009).

48. S. Yang, S. Choi, S. M. Jeon, and J. Yu, "Silica nanoparticle stability in biological media revisited," Sci. Rep. 1–9 (2018).

49. C. Pacholski, M. Sartor, M. J. Sailor, F. Cunin, and G. M. Miskelly, "Biosensing using porous silicon double-layer interferometers: Reflective interferometric fourier transform spectroscopy," J. Am. Chem. Soc. **127**, 11636–11645 (2005).